Geophys. J. Int. (2005) **160,** 651–666 doi: 10.1111/j.1365-246X.2005.02506.x

Seismic refraction evidence for steep faults cutting highly attenuated continental basement in the central Transverse ranges, California

Zhimei Yan,[1] Robert W. Clayton[1] and Jason Saleeby[2]

[1]*MS* 252-21, *Seismological Laboratory, California Institute of Technology, Pasadena,* CA 91125, *USA.*
E-mails: yanmei@gps.caltech.edu (ZY); clay@gps.caltech.edu (RWC)
[2]*MS* 100-23, *Division of Geological and Planetary Sciences, California Institute of Technology, Pasadena,* CA 91125, *USA. E-mail: jason@gps.caltech.edu*

Accepted 2004 September 30. Received 2003 September 13; in original form

SUMMARY

A 2-D upper crustal structural profile with seven steeply dipping faults was constructed from the Los Angeles Region Seismic Experiment phase II (LARSE II) seismic refraction data recorded over the north central Transverse ranges and adjacent Mojave desert in southern California. The profile extends to a depth of approximately 4 km. The faults were identified from distinctive features in the seismic first arrival data, while the velocity structure was determined from travel times and refined by forward modelling. The resulting seismic velocity structure is correlative to the geological structure along the profile and is used to help constrain a geological cross-section. Six of the seven faults detected from the seismic data correspond directly to geologically mapped faults in the central Transverse ranges and adjacent Mojave desert. From south to north, they are the Pelona fault, the San Francisquito fault, the Clearwater fault, the San Andreas fault and two faults that cut the Portal ridge. The seventh fault is buried beneath Quaternary deposits of the western Mojave desert and appears to correlate with an additional fault that cuts Portal ridge out of the section line. The southernmost fault (the Pelona fault) separates the younger Vasquez formation in the south from the Pelona schist in the north and is determined to be an intermediate (40°–60°) south-dipping normal fault. This coupled with field observations indicate that the Pelona fault was instrumental in the late Oligocene—early Miocene formation of the Soledad basin, and the structural ascent and exhumation of the Pelona schist along the proto-Sierra Pelona intrabasin ridge. Analogous Neogene extensional deformation is found to have affected the western Mojave desert region, where faults 6 and 7 appear to have had north side down normal displacement and to have been instrumental in forming the western Antelope basin. A 6.0 km s^{-1} basal layer to our shallow seismic structure is correlated with the Pelona schist south of the San Andreas fault and with the tectonically related Rand schist beneath the western Mojave desert. Granitic and gneissic crystalline rocks, which form regional upper plate complexes along the Vincent thrust above the Pelona schist and along the Rand thrust above the Rand schist, yield consistently low seismic velocities as compared with the expected velocities for the constituent rock types. These anomalous velocities are reconciled by the degraded structural and textural state of the upper plate crystalline rocks that resulted from extreme shearing, brittle fracturing and related retrogressive hydration reactions starting during or shortly after the latest Cretaceous—early Palaeocene underthrusting of the schists. Extension, translation along the San Andreas transform system and compressional faulting with the uplift of the Transverse ranges further accentuated the basement deformations. The integrated result is that the survival of the Precambrian through Mesozoic granitic crust of the region became a rootless and highly attenuated upper crustal layer.

Key words: central Transverse ranges, crustal structure, finite-difference methods, LARSE II, steep faults.

1 INTRODUCTION

The Transverse ranges of southern California are a structurally complex region that records a protracted history of interactions between the North America Plate edge and the Farallon Plate and subsequently with the East Pacific rise with the demise of the Farallon Plate (Atwater 1989; Atwater & Severinghaus 1989; Atwater & Stock 1998; Crouch & Suppe 1993; Dickinson 1981,

1996; Jacobson *et al.* 1996; Nicholson *et al.* 1994; Ingersoll & Rumelhart 1999). The pre-Cenozoic basement rocks of the region record the subduction of the Farallon Plate along an Andean-type arc–trench system that can be traced continuously from the northern Sierra Nevada to the central Baja California regions (Crouch & Suppe 1993; Saleeby 2003). Late Cretaceous to Cenozoic rocks of the Transverse ranges, however, record a uniquely complex tectonic overprinting history on this regionally extensive Andean-type system. The first overprint entailed the latest Cretaceous—early Palaeogene subduction of a shallow segment of the Farallon Plate (Saleeby 2003). This resulted in the shearing off of the subcontinental lithosphere mantle beneath the corresponding segment of the magmatic arc and the tectonic emplacement of subduction accretion assemblages directly beneath rocks belonging to the axial region of the arc (Jacobson *et al.* 1996). These events not only profoundly affected the deep crust–upper-mantle regime, but also highly deformed rocks of the magmatic arc and disrupted depositional patterns of the adjacent forearc basin. The early Neogene encroachment of the East Pacific rise into the southern California Plate edge environment instigated yet another disruptive tectonic regime in what was to become the modern Transverse ranges. Most important are ~255 km of right slip on the San Andreas and ~60 km on the San Gabriel faults (Dickinson 1981, 1996).

This study focuses on a north–south transect across the north-central Transverse ranges and adjacent western Mojave desert. The principal geographic features of the Transverse ranges that are traversed include the Santa Susana—San Gabriel mountains transition in the San Fernando pass area, the Santa Clarita valley and the adjacent westernmost Soledad basin, the Sierra Pelona, the Liebre and Sawmill mountain blocks, and the Portal ridge (Fig. 1). Basement rocks along this transect are part of the greater San Gabriel mountains igneous and metamorphic complex of Precambrian and Mesozoic age, and Mesozoic magmatic arc rocks of the western Mojave desert. Both of these basement complexes record shallow slab segment subduction along the regionally extensive Vincent and Rand thrust systems (Cheadle *et al.* 1986; Li *et al.* 1992; Malin *et al.* 1995; Jacobson *et al.* 1996; Fuis *et al.* 2001; Saleeby 2003). These thrust systems placed subduction accretion assemblages of the Pelona and Rand schists beneath Mesozoic magmatic arc rocks and their continental crystalline host rocks during latest Cretaceous—Palaeocene time. Scattered remnants of uppermost Cretaceous to mid-Eocene strata of the transect and of adjacent regions record subsidence of the Vincent–Rand thrust complexes to marine conditions in response to extensional collapse of the shallow slab segment orogen (Malin *et al.* 1995; Saleeby 2003). In late Eocene through much of Oligocene time, the study area sat in the forearc region of a diffuse magmatic arc that was well inland of the plate edge environment, which marks the re-establishment of subduction related magmatism in the wake of shallow slab segment subduction (Burchfiel *et al.* 1992; Saleeby 2003). Upper Oligocene to mid-Miocene strata of the region record extension and volcanism related to the encroachment of the East Pacific rise into the plate edge environment (Hendrix & Ingersoll 1987; Dickinson 1981). By mid-Miocene time, significant transrotations began to affect the region as the San Andreas transform system developed (Luyendyk *et al.* 1980; Luyendyk 1991; Bird & Rosenstock 1984; Hornafius *et al.* 1986; Humphreys & Hager 1990; Dickinson 1996). Further evolution of this system involves transpression that deformed and uplifted the Transverse ranges to their current active state.

The Los Angeles Region Seismic Experiment phase II transect (LARSE II) extends northwards from the Santa Monica mountains coast, through the Transverse ranges and western Mojave desert

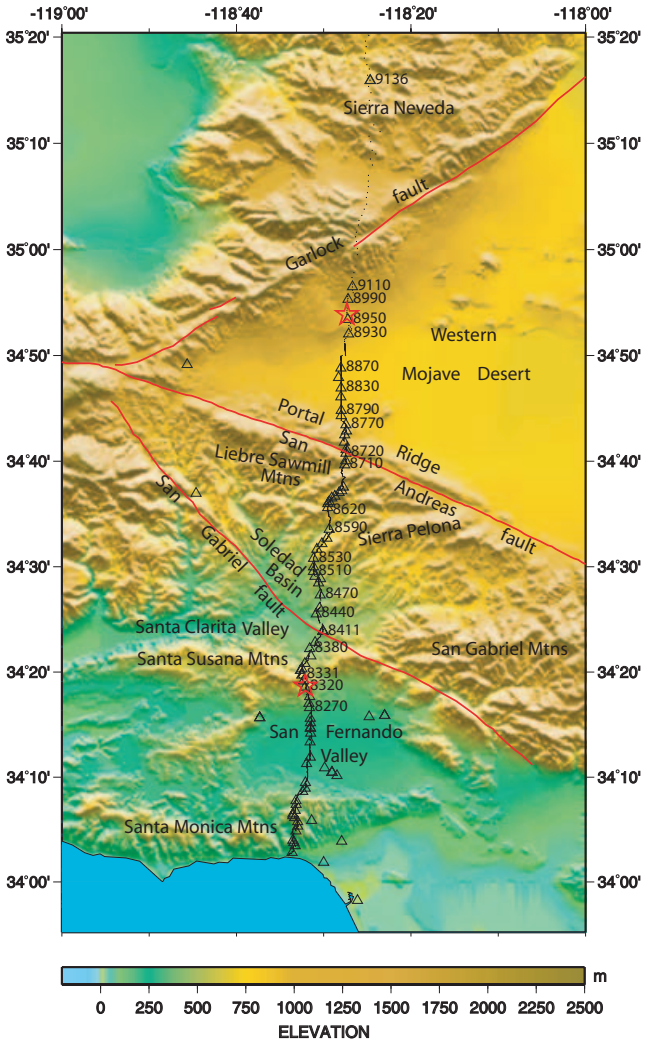

Figure 1. Topographic relief in southern California. Triangles represent shots with shot numbers of several selected shots beside them. Shot numbers generally increase from south to north. Little dots are receivers. Nearly 100 shots and 1400 receivers were deployed along the main line. Two stars represent the end points of the profile in this study.

and into the southernmost Sierra Nevada. It provides a large-scale, high-resolution seismic data set across the Transverse ranges part of the modern plate edge. Along the main line of the survey, over 1000 seismographs were deployed at 100 m spacing and shot points were spaced approximately 1 km apart (Fig. 1). The focus of this paper is on the segment that runs between the San Fernando pass and the western Mojave desert. In this paper, we present the inversion of the upper crustal structure based on first arrivals of a sequence of shots from the Santa Susana mountains to the western Mojave desert. Of particular interests are the identification of major faults and construction of a 2-D velocity structure model. This 2-D structure can be correlated to the first-order structural features that record the geological development of the region. Most importantly, the 2-D seismic structure model resolves several well-mapped faults, which include the Pelona, San Francisquito, Clearwater and San Andreas faults. Each of these faults is known to cut basement and to juxtapose fundamentally different rock types at the surface of the Earth. The 2-D structure model places constraints on the geometry of these and other recognized faults at depth, as well as on the pre-existing

regional structure cut by these steep faults. These constraints are used in the construction of a geological cross-section along the seismic line, which is constructed mainly from published mapping and our own unpublished topical mapping.

2 ANALYSIS OF THE REFRACTION DATA

The first arrivals on the LARSE II survey generally appear as three branches as is evident on a typical shot gather shown in Fig. 2. The first branch has a velocity of 2.0–2.5 km s^{-1} and is the result of a slow sedimentary layer that is prominent in the San Fernando valley and the Mojave desert. The second branch is the result of broken upper plate basement rocks and Early Neogene to Cretaceous sedimentary rocks and has a velocity around 4.0 km s^{-1}. The final segment has a velocity of 6.0 km s^{-1} and is the normal mid-crustal velocity in southern California. Of particular interest in the first arrival data is the reverse branch that is labelled as AB in Fig. 2. The slope of this segment implies an apparent velocity that is too large to be a reasonable velocity for the study area. This feature is prominent on all south-to-north profiles across the Santa Clarita valley (see Fig. 3, shots nos 8331 to 8520). It is fixed to the same ground point rather than a particular source–receiver offset. On the reverse profile through this region (north to south), the travel time curves all converge to a single 3.5 km s^{-1} branch. This velocity is lower than that of the near offset part of shot no. 8590. These two features are characteristic of an abrupt lateral change in properties that is usually caused by a steep fault. In this case, it is the Pelona fault that juxtaposes slow Vasquez formation on the south against the fast Pelona schist on the north.

In order to study the typical signatures that a fault imparts on first arrivals and to provide a method to invert velocity structure from these anomalous first arrivals, a simple faulted two-layered model is examined. Synthetic arrival times from 17 shots were calculated using an acoustic finite difference method. The model and two synthetic seismograms that illustrate the above two features

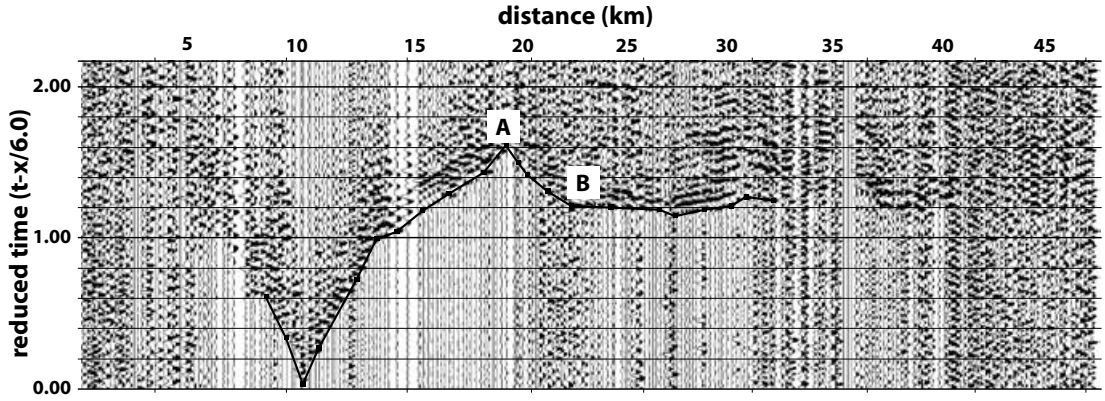

Figure 2. One typical shot gather (no. 8411) in the study area. Travel times are reduced by 6.0 km s^{-1}. Black line is the first arrival picks. The first arrival branch of no. 8411 has three normal segments, which have positive or zero slopes. Velocities of the three segments are 2.4, 4.3 and 6.0 km s^{-1}, respectively. The unusual thing about this shot gather is the negative slope segment (AB) between the second and third segments, which indicate an apparent velocity too large to be a reasonable true velocity for the study area.

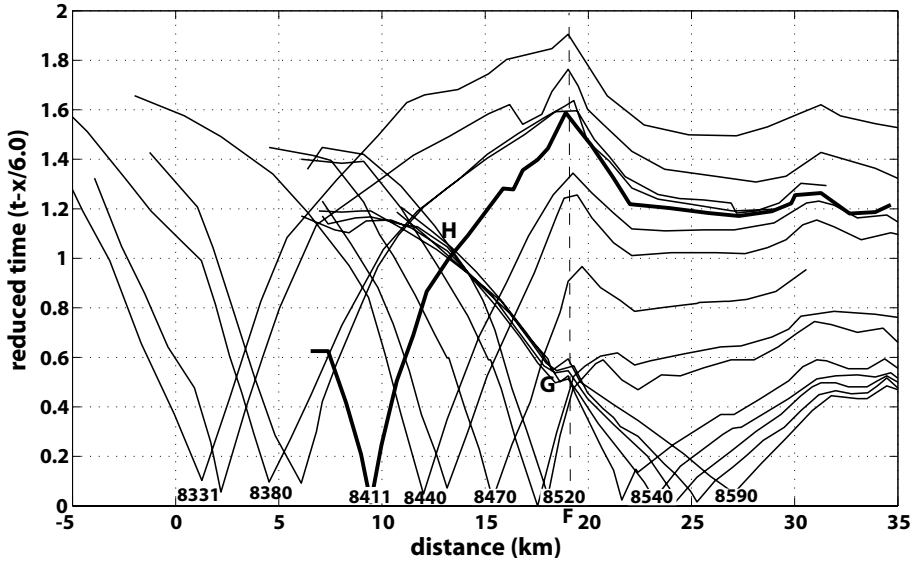

Figure 3. First arrivals for a sequence of shot gathers. The heavy solid line represents first arrival picks for the previous shot no. 8411. A negative-slope segment exists on every shot south of no. 8520, a peak point thus appears and they are almost aligned to the same ground point. For shots north of shot no. 8520, first arrivals of their south branches converge with each other to the south of the fault and adopt a similar low velocity (GH). The above two features are both offset-independent, but location-dependent, indicating the existence of an abrupt lateral velocity change around shot no. 8520.

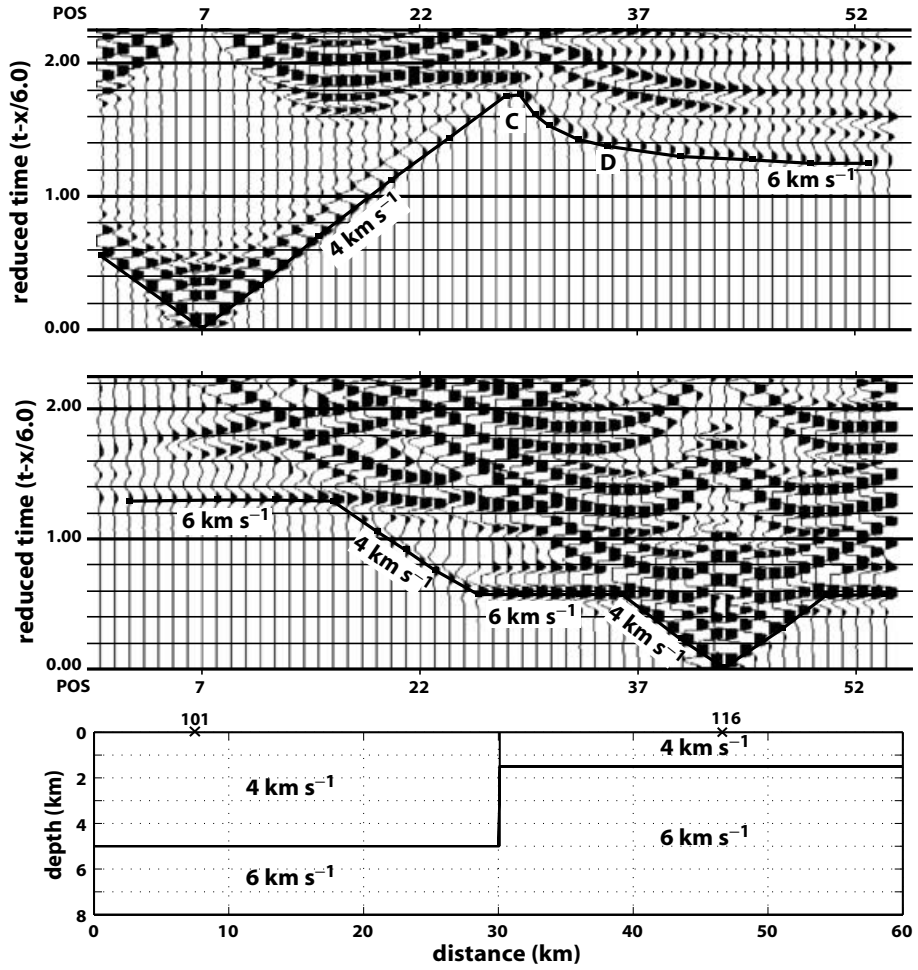

Figure 4. A single faulted one-layer over a half-space velocity model and two synthetic seismograms for two shots on either side of the fault. Synthetic waveforms were computed using a full waveform finite-difference method. In the bottom panel, x on the top surface of the model represent the two shots. Synthetic seismograms of the two shots are shown in the top and middle panels. The top one is the synthetic seismogram for shot no. 101, which is on the footwall. The negative-slope segment feature (CD) similar to AB of shot no. 8411 is observed to the right of the fault. The middle panel is the synthetic seismogram for shot no. 116, which is on the hangingwall. The unusual low-velocity segment (the second 4 km s^{-1} segment away from the shot) is observed to the left of the fault.

are shown in Fig. 4. The upper panel shows the synthetics for a shot on the footwall. It shows the prominent negative-slope branch CD similar to AB in the real data (Fig. 2). This reverse branch exists on all the shots far away from the fault on the footwall (see Fig. 5). The middle panel shows the synthetics for a shot on the hangingwall. It has an unusual velocity variation pattern, which is closely related to the fault. The apparent velocity changes from 4.0 to 6.0 km s^{-1}, then back to 4.0 km s^{-1} and 6.0 km s^{-1}. Left branches of the first arrivals for all the shots on the hangingwall (see Fig. 5) share similar velocity variation patterns and the second 4 km s^{-1} branch (unusual low-velocity branch) all converge to each other on the footwall side of the fault. This convergent unusual low-velocity branch feature matches the convergent segment labelled as GH in the real data (Fig. 3). A third feature that a fault imparts on first arrivals is a group of apparent head wave branches like L1, L2, and L3 in Fig. 5, whose arrival times increase systematically with distance away from the fault. They occur on shots close to the fault on the footwall. Feature F2 exists on the opposite side of the fault from features F1 and F3. These three features are useful in identifying faults from the seismic data and a further explanation of them is given in the Appendix.

Using the three features described above, we identified six faults from the central Transverse ranges and western Mojave desert portion of the LARSE II line. First arrivals for several selected shots and the identified faults are shown in Fig. 6. Features related to faults in the real data are not as obvious as that for a single faulted situation because the patterns for neighbouring faults interact with each other. However, each fault we identified has its corresponding diagnostic features, with fault 1 having the most obvious features. It has both the negative-slope segments for shots from the south side and the convergent low-velocity segments for shots from the north side, indicating that a large velocity contrast occurs across this fault and low-velocity materials accumulated on the south side. Features related to faults 2, 3 and 4 are not obvious as a result of strong interaction effects, but we can see the systematic increasing pseudo–head-branches related to faults 3 and 4 for shots from the south and north side, respectively, and the low-velocity segments related to faults 2 and 3. The features indicate that higher velocity material (a shallower interface) exists between faults 3 and 4, while lower velocity material (a deeper interface) is present in the blocks between faults 2 and 3, and between faults 4 and 6. Low-velocity segments are obvious on the north side of both faults 6 and 7 in the

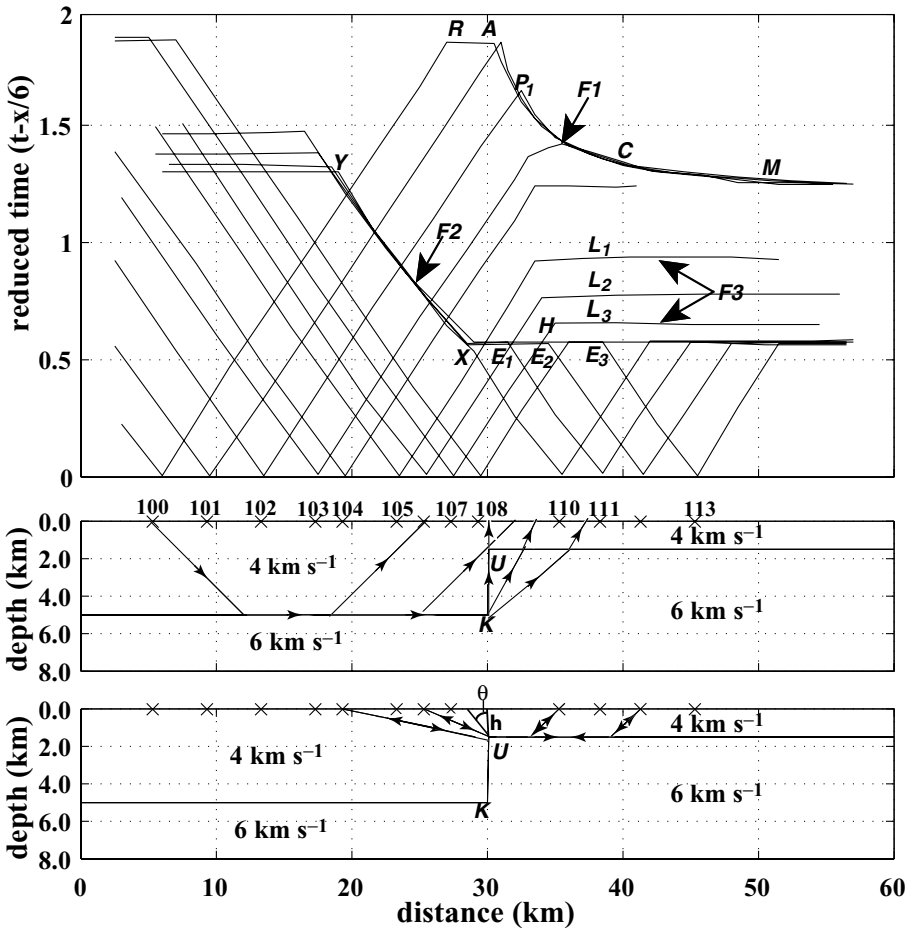

Figure 5. Velocity structure and first arrival picks for the single faulted one-layer over a half-space model. Velocity structure with typical ray paths for the first arrival phases of the three groups of shots is shown in the middle and bottom panels. First arrival picks are shown in the top panel. The first arrivals show three features (F1, F2 and F3) that are diagnostic of a fault. F1: negative-slope segments (AC); time decreases with offset along this segment and a peak point shows up; it exists on shots on the footwall far away from the fault. F2: convergent unusual low-velocity segment (XY); first arrivals of a sequence of shots adopt a similar low velocity and converge with each other along this segment; they exist on shots from the hangingwall. F3: systematic time-increasing pseudo–head-wave branches; they exist on shots from the footwall close to the fault (shot nos 105, 107 and 108); apparent kink points of these shots are not depth-dependent, but related to the shot distance away from the fault instead. Typical ray paths for shots far away from the fault on the footwall are shown in the middle panel. Note that the rays that first travel along the left interface then diffract from point K are the rays that produce the negative-slope segments (F1). Hence, the negative-slope segment does not represent a true velocity of the sampled area. In the bottom panel, the rays that first travel along the right interface then diffract from point U are the rays that appear as convergent low-velocity segments (F2) for shots from the hangingwall. Rays that travel along the same path, but reverse direction, i.e. for shots on the footwall, appear as the systematic time-increasing pseudo–head-wave branches (F3). Here h is the top layer thickness of the hangingwall. θ is the critical angle.

Mojave desert, indicating a relative accumulation of low-velocity sediments on the north side of both faults.

In this densely faulted area, a number of the first arrival kinks appear as a result of lateral velocity variations, so care is needed when using the kinks to estimate thickness of layers. In this study, thickness of layers is assumed to remain almost constant between faults and the kink points, which are least influenced by lateral velocity variations, are used to estimate the thickness. Usually, the kink point of the farthest shot away from the fault is used. For example, for the block south of fault 1, only the second intercept point of the north branch of shot no. 8331 is used to calculate the thickness of the second layer. The kink point of the nearest shot to the fault on the footwall is also used to estimate the layer thickness for the hangingwall. For example, the kink point for the north branch of no. 8590 is used to determine the thickness of the block between faults 2 and 3. The influence of faults on first arrival branches and the rational behind our kink point selection process are discussed in the Appendix. The shallow velocities are determined from the near offset part of the first arrival data. The velocity of the second layer is assumed to be 6.0 km s^{-1} in the central area. The resulting model is shown in Fig. 6.

In order to test the validity of this method, arrivals of several shots from the top surface of this velocity structure are computed using an acoustic finite-difference method. The acoustic approximation is used because the data is recorded on vertical seismometers and the sources are explosions, which means that the main energy recorded by the seismometers is *P* waves. The finite difference method can handle models of arbitrary complexity. Comparison of the synthetic first arrivals of several selected shots with the observed data for corresponding shots is shown in Fig. 7. From these, we can see that synthetic first arrivals match the large-scale features of the data at far offsets and compare well with the details of the observed data

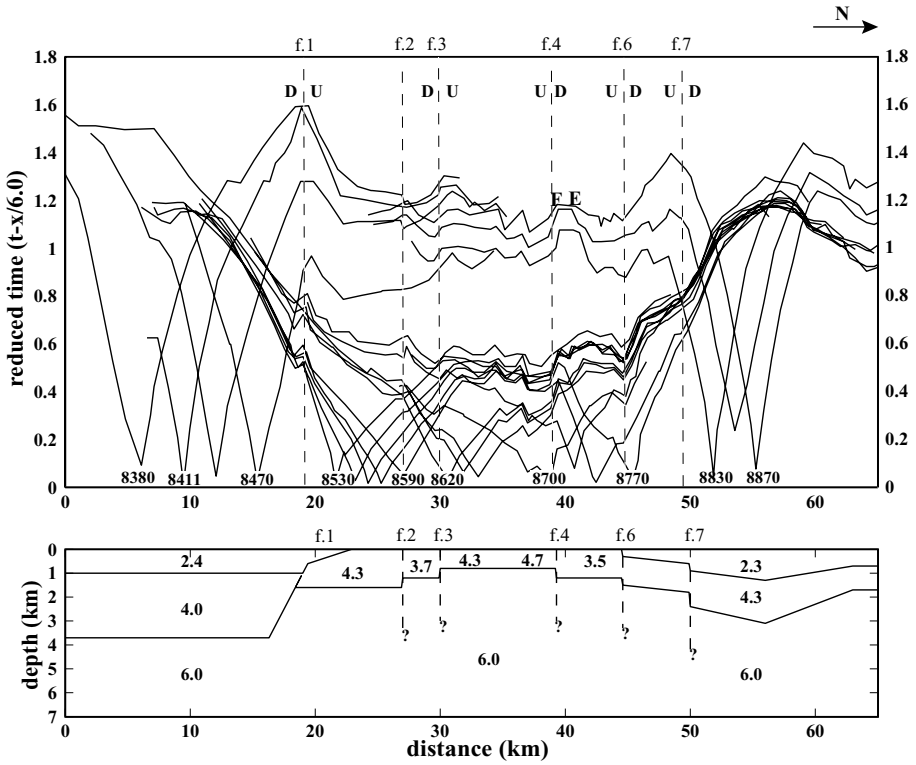

Figure 6. The upper panel is the first arrival picks of several selected shots (with shot numbers beneath) for the study area and the bottom panel is the preliminary velocity structure inverted from the first arrival data. Six faults were identified from the three distinctive features in the arrival time data. Each identified fault has its own characteristic features though attributes related to fault 1 are the most prominent. U or D on either side of the faults represents the hangingwall (shallower interface) or the footwall (deeper interface), respectively. Thickness of the velocity layers is estimated from appropriate crossover points under the assumption that thickness of the layers does not change significantly between faults. The dip angle of fault 1 is determined to be around 40°–60° to the south. A question mark is put beneath each fault because the depth extension is indeterminate.

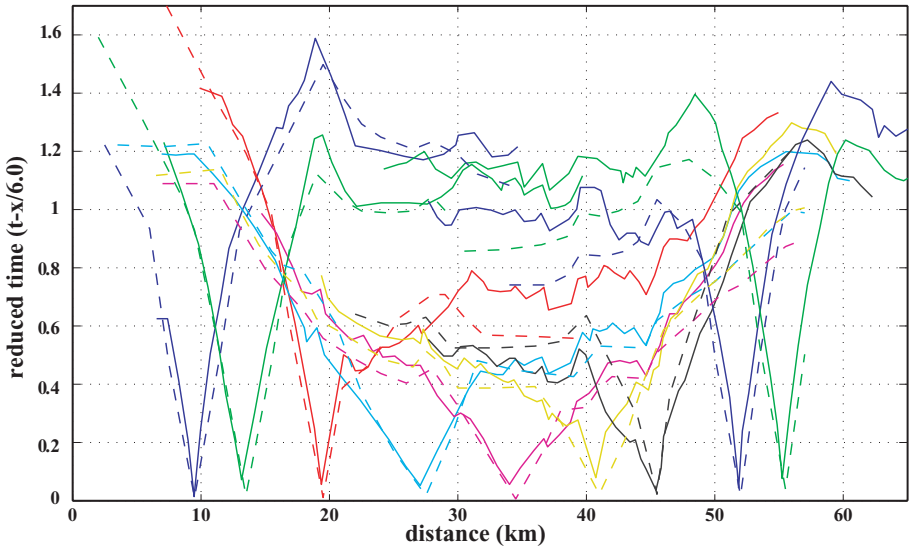

Figure 7. Comparison of synthetic first arrivals (dashes) for several shots from the preliminary model in Fig. 6 with the observed arrivals (solid) of corresponding shots. The synthetics generally fit the data well in the near offset. Big features similar to the real data show up in the far offset, but arrival times are poorly modelled.

at near offsets. However, the arrival times at far offset are poorly modelled, which means that we need to further refine the deeper structure.

To further refine the structure by including the far offset part of the data, we find that we need to accurately correct the influence of topography. Topography is relatively flat in the southern and northern parts of the study area, but varies substantially in the central part. The elevation increases by 0.6 km in less than 10 km distance and the arrival time changes by 0.15–0.3 s accordingly. The standard static elevation correction does not work well for such rapid variations. To

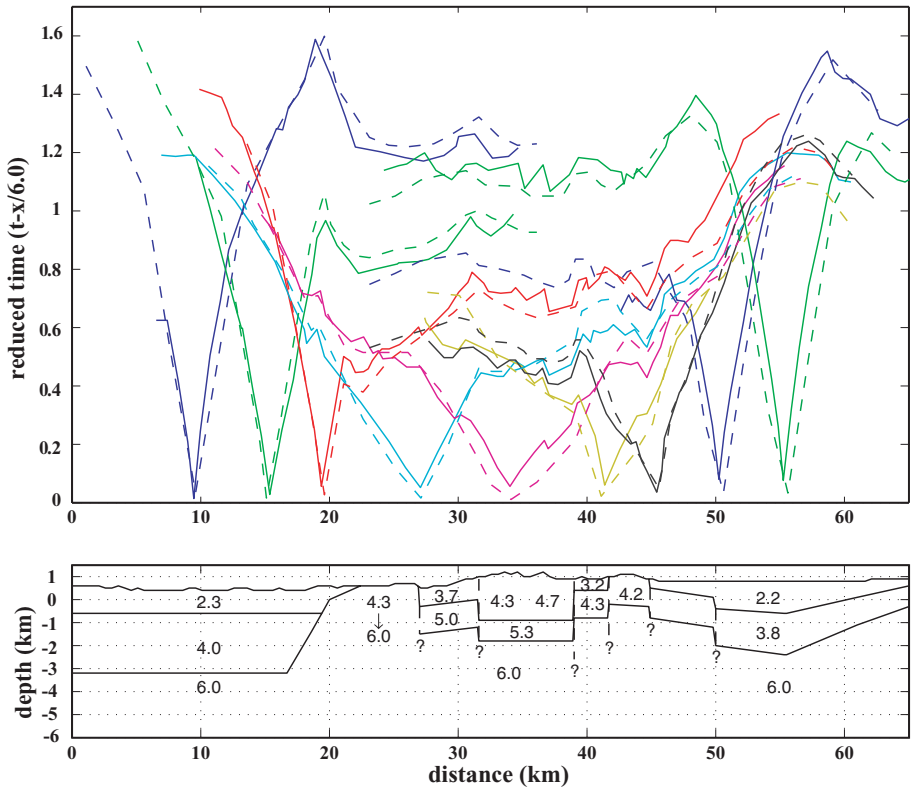

Figure 8. Comparison of synthetic first arrivals (dashes) for several shots from the improved model from trial and error modelling with the observed data (solid) of corresponding shots. The fit between the synthetics and the observed data, especially at far offset, is significantly improved compared with the preliminary model.

properly account for topography, we added variations in the source and receiver elevations into the finite-difference modelling program. We then refine the model by trial and error modelling until the fit of the synthetics to the data is significantly improved. The resulting model and comparison of the synthetic first arrivals with data are shown in Fig. 8. The major difference between this model and the preliminary one is that we add a second layer with a velocity around 5.0 km s^{-1} in the Liebre–Sawmill mountain block (from 27 to 38 km in Fig. 8) because all the synthetic first arrivals from farther shots for the preliminary model are faster than the observed data in this area.

With this further refinement, we find that an additional fault (fault 5) exists to the north of San Andreas fault and that rocks between these two faults have relatively low velocity. In the area near the San Andreas fault (around 40 km in Fig. 6), the first arrivals for several shots from the Mojave desert are around 0.1 s slower than that in the surrounding area, such as segment EF in the first arrival curve of shot no. 8830. For shots from the south, such as nos 8530 to 8590 at distances from 20 to 28 km, first arrivals increase approximately 0.05 s across this narrow zone. From these features, we deduce that this narrow zone is a low-velocity zone. An additional fault (fault 5) bounds its north boundary. From our simulation, this zone is 2–2.5 km wide and extends to at least 1.5 km deep from the surface. This zone geologically corresponds to a fault sliver between the San Andreas fault and fault 5. It is associated with movements along the San Andreas fault and is characterized by highly fractured granitic basement rocks with zones of fault gouge.

In the Sierra Pelona (the block between 20 to 27 km in Fig. 8), the refracted wave increases in velocity with distance away from the Pelona fault (from shot nos 8510 to 8440), so we deduce that velocity increases with depth in this area. A linear gradient of the velocity from 4.3 km s^{-1} at depth 0.5 km to 6.0 km s^{-1} at depth 2.0 km significantly improves the fit to the data. In the Mojave desert, we find that a velocity value of 3.2 km s^{-1} for the second layer increases the fit of the synthetics for shots from nos 8530 to 8590, but the synthetic first arrivals for shots from nos 8770 to 8870 are too late compared with the data. A velocity value of 3.8 km s^{-1} gives an overall better fit. The refined velocity model is shown in Fig. 8.

Features related to fault 1 are very prominent (Fig. 3). It has both the negative-slope segments for shots from the south side and the unusual low-velocity segments for shots from the north side. The unusual attribute about this fault is that the peak points of the regressive segments are almost aligned to the same ground point, instead of being distributed along a diffraction curve for a vertical fault (compare with Fig. 5). As discussed in the Appendix, relative location of the peak point and the kink point indicates that this fault is moderately dipping to the south. A dip angle around 40°–60° makes the synthetic first arrivals best fit the data. The best-fitting model and synthetic first arrivals for several shots are shown in Fig. 9. Peak points of the regressive segments in the synthetic data are almost aligned, which matches the real data. So we deduce that dip angle of the Pelona fault is around 40°–60° to the south.

3 CORRELATION OF SEISMIC AND GEOLOGICAL STRUCTURE

The shallow crustal velocity structure deduced from the LARSE II seismic data is used to help constrain a geological cross-section constructed from published geological mapping and drill hole data

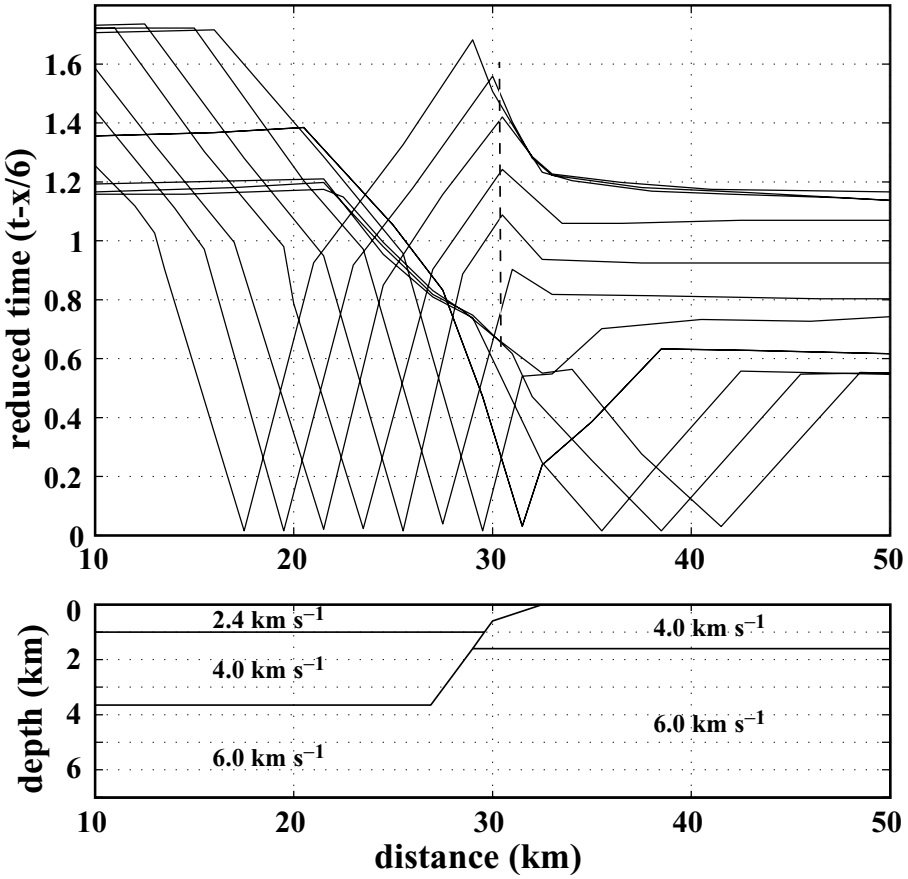

Figure 9. Synthetic first arrivals of the best-fitting model for the real data set shown in Fig. 3 related to the Pelona fault. The fault here dips to the south at an angle of 45°. Note the kink points for the shots south of the fault are almost aligned to the same ground point, similar to the observed features in real data. The similarity between these two arrivals indicates that this fault dips to the south and the dip angle is around 45°.

(Dibblee 1967, 1982a, 1982b, 1992, 1996, 1997a,b; Wright 1991), and our own topical mapping (Saleeby, unpublished data). The geological section and seismic velocity section are shown at 1:1 scale along with a geological strip map in Fig. 10. All the faults interpreted from the LARSE II seismic data have corresponding structures in field and are shown on the cross-section. From south to north, they are the Pelona fault (1), the San Francisquito fault (2), the Clearwater fault (3) the San Andreas fault (4) two unnamed faults (5, 6) that cut Portal ridge and a buried fault (7) in the adjacent Mojave desert. Velocity values determined from seismic data can be compared with the general rock types and their textural states in the geological cross-section, recognizing that in some areas there are thickness and velocity trade-offs in the seismic structure. Additionally, the Fig. 10 cross-section correlates our shallow velocity structure for the western Mojave desert region with buried fault and basin structure determined along the nearby Mojave desert Consortium for Continental Reflection Profiling (COCORP) 1 line (Li *et al.* 1992). Resolution of fault structures in the southern Santa Clarita valley to San Fernando pass region is poor for this segment of the LARSE II data that we have processed, a point that we will return to below.

The most distinctive structure that our LARSE II data analysis has resolved is the Pelona fault (Fig. 10). Pelona schist has moved up along the footwall of this fault relative to hangingwall strata of the Soledad basin. The Soledad basin is defined as a depocentre principally by a thick (locally up to 5000 m) section of volcanic and alluvial deposits of the upper Oligocene—lower Miocene Vasquez formation (Hendrix & Ingersoll 1987). The surficial low-velocity lens that extends northwards over the Pelona fault corresponds to upper Miocene strata that unconformably overlap the Vasquez formation as well as lap across the western end of the Pelona fault. The Pelona fault was thus rendered inactive by upper Miocene time. From our study, we have determined that this fault dips between 40° and 60° to the south placing the Vasquez formation in the hangingwall above footwall Pelona schist. Field observations of the fault as exposed several kilometres east of the transect line indicate that it has had a complex movement history involving mainly south side down normal displacement. Thin selvages of cataclastic granitic rock lie along the fault between the schist and the Vasquez formation. We interpret these to be disrupted vestiges of the Vincent thrust upper plate, which was attenuated in part by the extension related to the Pelona fault. Normal displacement along this fault is interpreted to have begun during late Oligocene—early Miocene formation of the Soledad basin. This fault appears to have been instrumental in the formation of internal sub-basins within the Soledad basin with the uplift of the proto–Sierra-Pelona as an intrabasin ridge (Muehlberger & Hill 1958; Hendrix & Ingersoll 1987). Hangingwall basement rocks above the Pelona fault were broken by north-dipping imbricate normal faults, which also gave the floor of the Soledad basin considerable topographic and structural relief. Footwall rocks of the Pelona schist are deformed into a broad antiform, which is interpreted to have developed by isostatically driven uplift and attendant flexure in response to crustal unloading along the fault (*cf.* Wernicke & Axen 1988). Net extension by normal displacement along the Pelona fault and attenuation of upper plate basement rocks

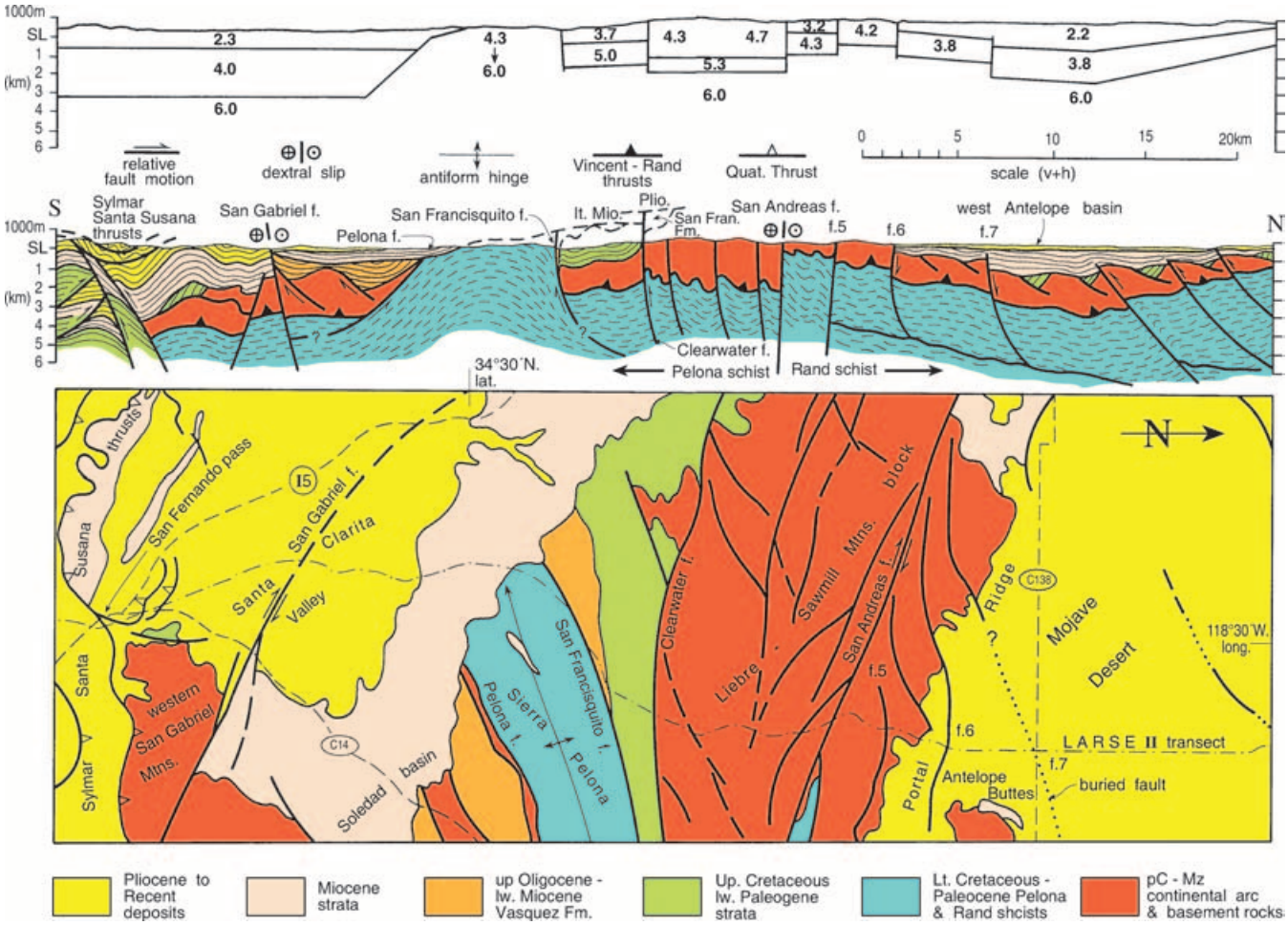

Figure 10. Shallow crustal seismic velocity structure, geological cross-section and geological strip map drawn at 1:1 scale along northern segment of LARSE II transect. Geology is after Dibblee (1967, 1992, 1996, 1997a,b) and Saleeby (unpublished data). Geological cross-section is registered in space to surface or near surface expression of steep faults imaged by seismic refraction data. Structure under the Mojave desert is diagrammatic and in part constrained by projection of the COCORP Mojave desert line 1 data onto the section plane (after Li *et al.* 1992). Location of LARSE II transect is shown by the dot-dash line. Locations of Interstate 5, and California State routes 14 and 138 are shown by dashed lines. Note that north is to the right in strip map.

beneath the Soledad basin may have been large (15 km) considering that Vasquez formation strata lie conformably on the Palaeocene San Francisquito formation north of the Sierra Pelona, but are unconformable on denuded upper plate basement rocks to the south.

The northern margin of the Sierra Pelona is bounded by the San Francisquito fault (fault 2), which is shown to be a steep structure by both the LARSE II seismic data and its linear geomorphic expression along much of its length. Locally, however, it assumes an ~70°N dip with hangingwall Tertiary strata dropped down relative to the footwall Pelona schist. This fault is constrained to be upper Oligocene—early Miocene in age by its cutting of the Vaquez formation and its depositional overlap by the same upper Miocene strata that lap across the Pelona fault (see the attached geological map in Fig. 10). Our interpretation of the San Francisquito fault is that it was an intra-Soledad basin normal fault, which in part accommodated the rise of the Sierra Pelona ridge and was instrumental in the partition of the basin into sub-basins. As discussed below, however, the San Francisquito fault may have been inverted to a modest high-angle reverse slip fault during the mid-Miocene demise of the Soledad basin as a distinct depocentre.

The relationship between the velocity structure and the geological structure of the Sierra Pelona is of significance. A velocity gradient from a surficial value of 4.3 to 6.0 km s^{-1} at ~ 2 km depth is resolved in the LARSE II data. The geological structure consists of a broad west-plunging antiform. The LARSE II transect crosses the western envelope of the antiform where fractured metaclastic rocks dominate the surface exposures. To the east along the core area of the antiform, metabasaltic rocks are more abundant and, at the deepest exposed structural level, weakly schistose amphibolitic metabasalt with relict pillow structures is well exposed. Laboratory measurements of average *P*-wave velocities for the Pelona schist sampled in the eastern San Gabriel mountains range from 5.8 km s^{-1} for metaclastic rocks to 6.4 km s^{-1} for metabasaltic rocks (Pellerin & Christensen 1998). Accepting that the relatively low metaclastic surface velocities of 4.3 km s^{-1} reflect the fractured and related weathered state of the surficial schist exposures, the geological structure of the Sierra Pelona antiform correlates quite well with the LARSE II and laboratory velocity data. The shallow metaclastic-rich envelope of the antiform yields low velocities, whereas the deeper more metabasaltic core yields higher velocities.

The block between the Sierra Pelona north bounding San Francisquito fault and the San Andreas fault (fault 4) consists of two eastward tapering structural wedges (Fig. 10). The first wedge lies between the San Francisquito fault and the steeply dipping

Clearwater fault (fault 3), and consists of folded Tertiary strata with an unconformable inlier of gneissic and granitic basement. The second wedge lies to the north between the Clearwater and San Andreas faults. It constitutes the Liebre—Sawmill mountain block and consists of highly fractured and faulted gneissic and granitic basement with small unconformable infolds of the Tertiary strata. The juxtaposition of basement rock with infolds of cover strata against the same cover strata with a basement rock inlier indicates an important north side up slip component for the steeply dipping Clearwater fault. This presumably occurred in conjunction with the folding of the Tertiary strata and its basement. The Clearwater fault dies out up section within overlapping Pliocene strata to the west of the study area and merges eastwards with the San Francisquito fault. The Liebre—Sawmill mountain block is characterized by numerous steeply dipping internal faults and a near pervasive steeply dipping brittle–ductile shear fabric. These basement rocks and the equivalent basement inlier within the adjacent sediment wedge are also interpreted as part of the attenuated upper plate of the Vincent thrust. The low seismic velocities deduced from the LARSE II data for surface exposures of these rocks (4.3 to 4.7 km s^{-1} and also 5.0 km s^{-1} for rocks beneath the Tertiary strata) as compared with laboratory velocities measured on more coherent samples scattered throughout the San Gabriel mountains basement complex (5.7 to 6.2 km s^{-1}; Pellerin & Christensen 1998) are reconciled by the highly degraded textural state of the Liebre–Sawmill basement rocks. The interface from the 5.0 km s^{-1} layer to the 6.0 km s^{-1} layer beneath the sediment wedge is correlated with the Vincent thrust. The deformed remnants of the thrust are in turn displaced up along the Clearwater fault and are correlated with the 5.3 km s^{-1} layer of the Liebre—Sawmill mountain block. This velocity is interpreted as the mark of superposed deformation and retrograding of both the upper and lower plates along the thrust. To the south of the San Francisquito fault, the Vincent thrust has been completely eroded away above the Sierra Pelona antiform. Significant erosional breaching through the upper plate began by mid-Miocene time as indicated by the appearance of appreciable schist detritus in the sedimentary record. Local breachment by late Oligocene—early Miocene time is indicated by rare schist clasts in the Vasquez formation (Muehlberger & Hill 1958; Saleeby, unpublished data).

Open folding of the Vasquez formation and its San Francisquito formation/granitic basement substrates marks the disruption of the Soledad basin in Miocene time. These events are accentuated by the middle to upper Miocene unconformity shown on the geological cross-section. Structural relations in the Vasquez formation suggest that the proto–Sierra-Pelona intrabasin ridge acted as a structural buttress during this compressional deformation. Adjacent to both the Pelona fault and the San Francisquito fault the otherwise openly folded Vasquez formation is rotated to near vertical and steeply overturned dips. Modest tightening and the development of second-order open folds (not present in the cross-section plane) in the Sierra Pelona antiform may have accompanied folding of the Vasquez cover strata. Inversion of the San Francisquito fault to a modest reverse slip component is also considered to have accompanied this folding event as suggested by the adjacent overturning of the Vasquez formation. The steeply dipping shear fabric and internal faults of the Liebre—Sawmill mountain block in general parallel the axial planar trend of folds in the cover strata. The implicit strain of this fault and rock fabric system appears much greater than that exhibited by the open folding of the cover strata. This suggests that the fabrics, and perhaps the faults, are inherited from earlier tectonic regime(s) and that perhaps they too have inverted their kinematic role from earlier extensional to later compressional behavior. The tapering of the Liebre—Sawmill mountain basement wedge and the adjacent San Francisquito formation wedge into the proximity of the San Andreas fault raises the possibility that the San Francisquito and Clearwater faults once had significant strike-slip components as part of the early San Andreas transrotational regime. Offset markers or shear sense indicators along these faults indicating such have yet to be observed, however. The Liebre—Sawmill mountain block is the highest topographic feature of the region by roughly 500 m. This is interpreted as the mark of uplift related to the late Neogene compressional deformation as well. The San Francisquito and presumably the Vaquez equivalent strata were eroded off the basement block as it was uplifted.

The geological analysis of the velocity structure offered above begs the question as to what is the appropriate average *P*-wave velocity for the Pelona schist? In their analysis of laboratory seismic velocity data, Pellerin & Christensen (1998) assumed a 9 to 1 ratio of metaclastic to metabasaltic rocks and derived an average *P*-wave velocity of 5.8 km s^{-1}. This lithologic ratio is too high for the core area of the Sierra Pelona, which could be more representative of the schist at depth. An average *P*-wave velocity of 6.0 km s^{-1}, as suggested by this study, appears more appropriate, although large transposed layers of pure metaclastic or pure metabasaltic rocks could yield velocity domains that deviate significantly in either direction from this value. Average *P*-wave velocities in the range of 6.2 to 6.5 km s^{-1} for the schist and 5.5 to 6.1 km s^{-1} for upper plate basement rocks were deduced for the Rand thrust complex of the Tehachapi mountains (Malin *et al.* 1995). The Rand schist in the Tehachapi mountains contains abundant metabasalt as well as the ubiquitous metaclastic rocks. The cogent point here is that depending on the actual metabasalt to metaclastic ratio of a given domain of the schist under investigation, it may or may not be distinguishable by seismic velocities from texturally and structurally coherent basement rocks of the respective upper plate (*cf.* Pellerin & Christensen 1998 Table 3).

The 6.0 km s^{-1} layer of our shallow crustal model to the southwest San Andreas fault is correlated to the Pelona schist. Such a correlation for the 6.0 km s^{-1} layer to the northeast of the fault, if correct, carries important implications for the geological interpretation of our shallower velocity structure model. Seismic reflection data for the western Mojave desert show the Rand schist at shallow crustal levels throughout much of the region (Cheadle *et al.* 1986; Li *et al.* 1992; Malin *et al.* 1995). These data also show the schist and its tectonically overlying granitic basement plate ramping up southwards towards the San Andreas fault. The ramping structure is confirmed by surface exposures of the schist in small hills ∼6 km north of the San Andreas fault, east of the study area, and by an ∼25-km-long fault sliver of schist lying along the north wall of the fault. This fault sliver underlies much of Portal ridge (Dibblee 1967) and the terminus of its surface exposure is 2 km southwest of the LARSE II transect (Fig. 10 map).

The 6.0 km s^{-1} basal layer of our shallow crustal model in the western Mojave desert is tentatively correlated with the Rand schist. As discussed above, the Rand schist is in regional tectonic terms correlative with the Pelona schist, although their immediate proximity as expressed along the LARSE II transect is a result of ∼255 km right slip on the San Andreas fault. The problem that arises from a simple correlation of the 6.0 km s^{-1} layer with the Rand schist is in the implied velocity of its upper granitic plate (3.8 km s^{-1}). As aberrant as this velocity seems, the presence of such basement rocks at depths that correspond to the boundary between our 2.2 and 3.8 km s^{-1} layers is corroborated by stratigraphic, drill home, gravity and seismic reflection data (Dibblee 1967;

Li *et al.* 1992). As discussed below, the geological structure of the 3.8 km s^{-1} layer is suggested to be highly complex, and characterized by shattered, retrograded and highly attenuated granitic basement rock.

Faults 5 and 6 constitute part of the high-angle fault system that obliquely transects Portal ridge. The surface exposures between the San Andreas fault and fault 5 consist of highly shattered granitic rocks with zones of fault gouge. These rocks correspond to the 3.2 km s^{-1} layer and the underlying 4.3 km s^{-1} layer is interpreted as highly fractured Rand schist projected beneath the shattered granitic rocks from schist exposures to the southeast. Surface exposures between faults 5 and 6 consist of shattered upper plate granitic rocks that correspond to the 4.2 km s^{-1} layer. Beneath these rocks at shallow levels presumably lies the Rand schist. The velocity variations between the faults 5 and 6 sliver and the San Andreas fault 5 sliver reflect the brittle deformation overprint of the San Andreas fault zone.

Fault 7 is buried beneath Quaternary deposits of the Mojave desert, but is well defined in the seismic data. Bedrock exposures in the nearby Antelope Buttes, to the east of the transect, correlate well with the seismic structure deduced between faults 6 and 7. The 2.2 km s^{-1} layer principally corresponds to a relatively thin section of Neogene strata exposed along the western edge of the Buttes and the 3.8 km s^{-1} layer corresponds to its underlying shattered basement. Fault 7 is correlated with a well-expressed fault that obliquely transects the western end of Portal ridge (Fig. 10 map). The correlation is based on the fact that the shattered granitic basement exposed to the north of the exposed fault constitutes the depositional substrate for a thick Neogene section. Fault 7 in the subsurface defines a basement scarp across which the Neogene section thickens abruptly. Thus, the stratigraphic changes that occur across the exposed fault, between the Antelope Buttes block and the western end of Portal ridge, match those seismically imaged across the buried fault 7: hence, the correlation.

The shallow seismic velocity structure deduced along the LARSE II line for the western Mojave desert region clearly defines the west Antelope basin, an east–west trending shallow trough that extends to the western tip of the Mojave desert (Dibblee 1967). Except for sparse drill hole data and gravity data (Dibblee 1967), and our shallow velocity model, constraints for the subsurface geological structure are sparse. The geological structure shown for the basin on Fig. 10 is constrained by these data and by the projection of COCORP seismic reflection data westwards onto the LARSE II transect from a parallel line located 10 km to the east of our transect. The COCORP data show a modest north-dipping fault, which corresponds spatially to the eastward extension of either fault 6 or 7. In addition to the Rand thrust ramping up to the south, the COCORP data also show a strong reflector internal to the schist that also ramps up to the south at a depth of $\sim$ 4 km beneath the thrust. Our interpretation is that faults 6 and 7 are basin bounding normal faults, which root into a detachment fault that corresponds to the reflector within the schist. Fault 5 may have had a similar origin, but it is shown on the cross-section as having been partly remobilized as part of the San Andreas fault zone. The COCORP data also show two distinctive north-dipping reverse faults at the northern end of their transect. These two faults and a third reverse fault, expressed as a dissected scarp and adjacent broad folding of Quaternary strata, are shown deforming the northern margin of the west Antelope basin. The northward ramping up of our shallow velocity structure under the northern west Antelope basin is attributed to this young, and possibly active, distributed compressive deformation. The COCORP data show additional north dipping faults, which appear to offset the top of the basement in an opposite sense as the reverse faults. These are interpreted as older basin floor normal faults.

The shallow 3.8 km s^{-1} layer that extends across the west Antelope basin floor merits special attention. Neogene stratigraphic thicknesses, sparse drill hole data and seismic reflection data (Dibblee 1967; Li *et al.* 1992) all point to this layer as upper plate granitic rock of the Rand thrust system. The 3.8 km s^{-1} velocity deduced for this layer seems excessively low, although velocities of 4.2 and 3.2 km s^{-1} were deduced for the apparent southward continuation of this layer where such basement rocks constitute the surface exposures. The interpretation offered here, and shown diagrammatically on the geological section, is that this layer is highly attenuated, shattered and retrograded upper plate granitic rock. This layer may also contain vestigial lenses of early Palaeogene strata, such as the Golar formation that is depositional on upper plate granitic rocks adjacent to the Garlock fault (Dibblee 1967). In this interpretation, these lenses have been dispersed by Neogene extension and overlapped along with their adjacent denuded basement by the Neogene basin fill. The extreme attenuation of the western Mojave desert upper granitic plate is considered a result of the superposing of Neogene extension over the effects of latest Cretaceous—early Palaeogene extensional collapse of the Rand thrust complex (*cf.* Saleeby 2003).

An alternative interpretation to that offered above for the 3.8 km s^{-1} layer is that it represents primarily a thick Palaeogene section of Golar formation affinity strata beneath the Neogene section. This is possible (*cf.* Saleeby 2003), but there are no surface exposures or drill hole data to support this view. In this interpretation, the Rand thrust would be opaque to our velocity data and it would perhaps correspond to the deeper reflector imaged by the COCORP data (Li *et al.* 1992). The favoured interpretation, however, is that most of the Palaeogene that may have existed beneath the west Antelope basin region has been removed by a combination of extensional tectonic denudation and erosion, and for the most part syn- and post-extensional Neogene strata of the basin lie unconformably on highly attenuated and shattered basement.

Final discussion focuses on the relatively simple seismic velocity structure derived for the southern end of our transect beneath the southern part of Santa Clarita valley and the San Fernando pass areas. As shown on the geological cross-section, the structure is much more complex than that of the seismic velocity model. Most notable is a lack of any signature neither for the San Gabriel fault, nor the Santa Susana—Sylmar thrust system. Nor is there any expression of the considerable basement relief beneath the Neogene strata of the area that is documented by drill hole data. In addition to the problem of poor resolution at the extremities of our seismic model, the most viable explanation for this is that upper plate crystalline rocks above the Vincent thrust of this region are also highly fractured and hydrated, and thus yield seismic velocities in a range below those of coherent basement rocks and overlapping with those of clastic sedimentary rocks. Such a textural state is born out by observations of crystalline rocks that constitute the western end of the San Gabriel mountains and that project westwards beneath the adjacent San Fernando pass area. As noted earlier, the history of upper plate crystalline rock fracturing, hydration and attenuation began during or shortly after initial schist underthrusting and has been accentuated by Neogene to Recent extensional, strike-slip and compressional deformations. The effects of this near pervasive textural and structural degradation of much of the southern California region crystalline basement are well expressed along the entire length of our transect by their consistently low *P*-wave velocities as compared with what

is known to typify texturally and structurally coherent continental basement rocks.

4 CONCLUSIONS

We recognized three characteristic features of faults in densely sampled seismic refraction data and these features were used to identify six faults in the north-central Transverse ranges and adjacent Mojave desert portion of the LARSE II transect. We also estimated the influence of faults (lateral velocity variations) on first arrivals, especially on kink points, which enables us to discriminate between different kinds of apparent kink points and to determine which apparent kink point is appropriate to derive a good estimate of *P*-wave velocity layer thickness. We locally used a simple 1-D depth-inversion method on these appropriate kink points to determine the thickness of different velocity layers for blocks between faults under the assumption that the thickness does not change dramatically between faults. A 2-D velocity structure was thus constructed as a preliminary model from the near offset part of the data. We then refined this preliminary model using test and trial modelling for the synthetic first arrivals to fit all the data. An additional fault (fault 5) was detected from this trial and error modelling. The synthetic first arrivals generally compare well with the recorded data. The velocity structure we constructed from the seismic data compare reasonably well with the known geological structure, constituent rock type and textural state data.

Locations of these seven faults are fairly well defined from the seismic data and they compare well to geologically mapped faults. From south to north, they are the Pelona fault, the San Francisquito fault (south and north bounding faults of Sierra Pelona), the Clearwater fault, the San Andreas fault, two faults associated with Portal ridge and a fault buried beneath Quaternary deposits within the western Mojave desert. Features related to the Pelona fault are most prominent and indicate that the velocity structure changes markedly across this fault from the Santa Clarity valley and underlying western Soledad basin to the Sierra Pelona.

The Pelona fault was an major active south-dipping normal fault during the late Oligocene—early Miocene formation of the Soledad basin. Footwall rocks of the Pelona schist were flexed into a broad open antiform probably as a result of isostatic response to crustal unloading along the Pelona fault. South side up normal displacement of the San Francisquito fault is interpreted to have in part accommodated the rise and flexure of the Sierra Pelona antiform. Between the San Francisquito fault and the San Andreas fault lies an elevated area characterized by intense brittle deformation of upper plate basement rocks of the Vincent thrust and the folding of its Tertiary cover strata. This block was folded and uplifted in mid-Miocene to earliest Pliocene time by compressive deformation probably in response to transpression along the San Andreas fault and as part of the regional uplift of the Transverse ranges.

The LARSE II transect in conjunction with COCORP reflection data of the western Mojave desert have identified structures that played a key role in the development of the west Antelope basin. The southern margin of this basin is controlled by steeply dipping Miocene (?) normal faults, which apparently root into a low north-dipping detachment surface. Mio-Pliocene basin fill thickens northwards across these normal faults. The northern margin of the basin is deformed by north-dipping reverse faults, some of which may be active.

The shallow crustal seismic velocity structure determined by the LARSE II data defines a regional pattern of surficial low-velocity sedimentary rock lenses, which represent the remnants of larger Cenozoic sedimentary basins. Constituent Palaeogene to lower Neogene strata were deposited and subsequently disrupted in extensional tectonic environments. Pliocene to Recent strata are deposited in the remnants of early Neogene extension-related basins, and are also in part deformed and uplifted along Pliocene to Recent compressive deformation zones. Our shallow seismic structure does not distinguish these contrasting settings for the Pliocene to Recent deposits. The Pelona and Rand schists form a basal high-velocity layer beneath the entire region at relatively shallow crustal levels. Between the schists and the Cenozoic strata lie highly attenuated, intensely fractured and variably hydrated remnants of the upper granitic crystalline plates of the Vincent and Rand thrust systems. These rocks consistently yield low *P*-wave velocities as compared with what would be expected for fresh coherent basement rocks. These low velocities reflect the highly degraded structural and textural state of the upper plate basement rocks in response to multiple extensional and subsequent compressive deformation events. Such degradation of these basement rocks is in places so extreme as to prohibit the seismic resolution of depositional contacts with their overlying Cenozoic cover strata.

In our analysis of the fault structure of the north central Transverse ranges and adjacent western Mojave desert, we have placed important constraints on vertical slip components. Neither the seismic data, nor the presence of offset geological markers or shear sense indicators in the study area has offered constraints on possible strike-slip components. The history of transrotation, transtension and transpression in the Transverse ranges region (Luyendyk 1991; Dickinson 1996; Ingersoll & Rumelhart 1999) leaves open the possibility of significant strike-slip components on some of the steep faults that we have resolved, in addition to that of the San Andreas fault.

ACKNOWLEDGMENTS

We thank the many volunteers who helped with the LARSE II experiment. We would like to thank Jascha Polet, Vala Hjorleifsdottir and Javier Favela for their reviews and comments. Helpful reviews by Walter Mooney and an anonymous referee are gratefully acknowledged. This research was supported by the Southern California Earthquake Center (SCEC). The SCEC is funded by NSF Cooperative Agreement EAR-0106924 and USGS Cooperative Agreement 02HQAG0008. This paper is SCEC contribution no. 736 and the Division of Geological and Planetary Sciences, Caltech, contribution no. 8972. JS acknowledges support under NSF grant EAR-0087347.

REFERENCES

Atwater, T., 1989. Plate tectonic history of the northeast Pacific and western North America, in *The Geology of North America: the Eastern Pacific ocean and Hawaii,* pp. 21–72, eds Winterer, E.L., Hussong, D.M. & Decker, R.W. The Geological Society of America, Boulder, Colorado, USA.

Atwater, T. & Severinghaus, J., 1989. Tectonic maps of the northeast Pacific, in *The Geology of North America: the Eastern Pacific ocean and Hawaii,* pp. 15–20, eds Winterer, E.L., Hussong, D.M. & Decker, R.W. The Geological Society of America, Boulder, Colorado, USA.

Atwater, T. & Stock, J., 1998. Pacific-North America Plate Tectonics of the Neogene Southwestern United States: An update, *Int. Geol. Rev.,* **40**(5), 375–402.

Bird, P. & Rosenstock, R.W., 1984. Kinematics of present crust and mantle flow in southern California, *Bull. geol. Soc. Am.,* **95,** 946–957.

Burchfiel, B.C., Cowan, D.S. & Davis, G.A., 1992. Tectonic overview of the Cordilleran orogen in the western United States, in *The Cordilleran*

Orogen: Conterminous US, pp. 407–427, eds Burchiel, B.C., Lipman, P.W. & Zoback, M.L., Geological Society of America, Boulder, CO, USA.

Cheadle, M.J. *et al.*, 1986. The deep crustal structure of the Mojave Desert, California, from COCORP seismic reflection data, *Tectonics,* **5,** 293–320.

Crouch, J.K., 1979. Neogene teconic evolution of the California Continental Bordland and western Transverse Ranges, *Bull. geol. Soc. Am.,* **90,** 338–345.

Crouch, J.K. & Suppe J., 1993. Late Cenozoic tectonic evolution of the Los Angeles basin and inner California borderland: A model for core complex-like crustal extension, *Bull. geol. Soc. Am.,* **105,** 1415–1434.

Dibblee, T.W., 1967. Areal geology of the Western Mojave Desert California, in *United States Geological Survey Professional Paper,* Vol. 522, pp. 1–98, ed. Dibblee, T.W. Jr., United States Government Printing Office, Washington, DC, USA.

Dibblee, T.W., 1982a. Geology of the Castaic Block, the Mountains and Hills Northwest of the San Gabriel Mountains, Southern California, in *Geology and Mineral wealth of the California Transverse Ranges,* Vol. 10, pp. 78–93, eds, Fife, D.L. & Minch, J.A., South Coast Geological Society, Santa Ana, California, USA.

Dibblee, T.W., 1982b. Regional geology of the Transverse Ranges Province of southern California, in *Geology and Mineral wealth of the California Transverse Ranges,* Vol. 10, pp. 7–26, eds Fife, D.L. & Minch, J.A. South Coast Geological Society, Santa Ana, California, USA.

Dibblee, T.W., 1992. *Geologic Map of the Oat Mountain and Canoga park (North 1/2) Quadrangles, Los Angeles County, California,* scale 1:24 000, map no. DF-36, Dibblee Geological Foundation, Santa Barbara, California, USA.

Dibblee, T.W., 1996. *Geologic Map of the Newhall Quadrangle*, Los Angeles County, California, scale 1:24 000, map no. DF-56, Dibblee Geological Foundation, Santa Barbara, California, USA.

Dibblee, T.W., 1997a. *Geologic Map of the Warm Springs Mountain Quadrangle*, *Los Angeles County*, *California*, scale 1:24 000, map no. DF-64, Dibblee Geological Foundation, Santa Barbara, California, USA.

Dibblee, T.W., 1997b. *Geologic Map of the Green Valley Quadrangle*, Los Angeles County, California, scale 1:24 000, map no. DF-65, Dibblee Geological Foundation, Santa Barbara, California, USA.

Dickinson, W.R., 1981. Plate tectonics and the continental margin of California, in *The Geotectonic Development of California,* pp. 1–28. ed. Ernst, W.G., Prentice-Hall, Englewood Cliffs, NJ, USA.

Dickinson, W.R., 1996. Kinematics of Transrotational Tectonism in the California Transverse Ranges and its contribution to cumulative slip along the San Andreas Transform system, *Geol. Soc. Am. Special Paper,* **305,** 1–46.

Ehlig, P., 1981. Origin and tectonic history of the basement terrance of the San Gabriel Mountains, central Transverse Ranges, in *The Geotectonic Development of California,* pp. 253–283, ed. Ernst, W.G., Prentice-Hall, Englewood Cliffs, NJ, USA.

Fuis, G., Ryberg, T., Godfrey, N.J., Okaya, D.A. & Murphy J.M., 2001. Crustal structure and tectonics from the Los Angeles basin to the Mojave Desert, southern California, *Geology,* **29**(1), 15–18.

Hendrix, E.D. & Ingersoll, R.V., 1987. Tectonics and Alluvial Sedimentation of the Upper Oligocene Lower Miocene Vasquez Formation, Soledad Basin, Southern-California, *Bull. geol. Soc. Am.,* **98**(6), 647–663.

Hill, D.P., 1982. Contemporary block tectonics: California and Nevada, *J. geophys. Res.,* **87,** 543–5450.

Hornafius, J.S., Luyendyk, B.P., Terres, R.R. & Kamerling, M.L., 1986. Timing and extent of Neogene tectonic rotation in the western Transverse Ranges, California, *Bull. geol. Soc. Am.,* **97**(12), 1476–1487.

Humphreys, E. & Hager, B.H., 1990. A kinematic model for the late Cenozoic development of southern California crust and upper mantle, *J. geophys. Res.,* **95,** 19 747–19 762.

Ingersoll, R.V. & Rumelhart, P.E., 1999. Three-stage evolution of the Los Angeles basin, southern California, *Geology,* **27,** 593–596.

Jacobson, C.E., Oyarzabal, F.R. & Haxel, G.B., 1996. Subduction and exhumation of the Pelona-Orocopia-Rand schists, southern California, *Geology,* **96,** 547–550.

Li, Y.G., Henyey, T.L. & Silver, L.T., 1992. Aspects of the crustal structure of the western Mojave Desert, California, from Seismic Reflection and Gravity data, *J. geophys. Res.,* **6,** 8805–8816.

Luyendyk, B.P., 1991. A model for Neogene Crustal rotations, transtension and transpression in Southern California, *Bull. geol. Soc. Am.,* **103,** 1528–1536.

Luyendyk, B., Kamerling, M. & Terres, R., 1980. Geometric model for Neogene crustal rotations in southern California, *Bull. geol. Soc. Am.,* **91,** 211–217.

Malin, P.E., Goodman, E.D., Henyey, T.L., Li, Y.G., Okaya, D.A. & Saleeby, J., 1995. Significance of seismic relfections beneath a tilted exposure of deep continental crust, Tehachapi Mountains, California, *J. geophys. Res.,* **100,** 2069–2087.

Muehlberger W.R. & Hill H.S., 1958. Geology of the Central Sierra Pelona, Los-angeles County, California, *Am. J. Sci.,* **256**(9), 631–643.

Nicholson, C., Sorlien, C.C., Atwater, T., Crowell, J.C. & Luyendyk, B.P., 1994. Microplate capture, rotation of the western Transverse Ranges, and initiation of the San Andreas transform as a low angle fault system, *Geology,* **22,** 491–495.

Pellerin, C.L.M. & Christensen, N.I., 1998. Interpretation of crustal seismic velocities in the San Gabriel-Mojave region, southern California, *Tectonophysics,* **286,** 253–271.

Saleeby, J., 2003. Segmentation of the Laramide Slab - evidence from the southern Sierra Neveda region, *Bull. geol. Soc. Am.,* **115**(6), 655–668.

Wernicke B. & Axen G.J., 1988. On the role of Isostasy in the Evolution of Normal-Fault Systems, *Geology,* **17**(9), 848–851.

Wright, T.L., 1991. Structural Geology and tectonic evaluation of the Los Angeles basin, California, *AAPG Mem.,* **52,** 35–134.

APPENDIX A: THE EFFECT OF FAULTS ON FIRST ARRIVALS

The complex patterns of first arrival branches resulting from a fault in a layer over a half-space model are shown in Fig. 5. For shot no. 100, the true crossover point for the interface on the left side of the model is at the point R. However, the existence of the fault causes an additional kink point at A, which is the transition point between the head wave travelling along the half-space boundary on the left side and the diffraction phase emanating from the point K in the model. The diffraction phase appears as a reverse branch in the first arrival time curve and this branch asymptotically approaches the half-space velocity on the right side of the model. As the shot nears the fault (i.e. nos 101 to 103), the true crossover point is not able to show up as a result of the sudden drop of the interface. The reverse branch, however, as the travel time for the diffraction phase from point K, shows up consistently, which gives rise to the pseudo–crossover-points, such as A and P1. This reverse branch (curve ACM) is the first characteristic feature of faults (F1). It is important to note that the highest point on the ACM curve should be used to estimate the layer thickness of the footwall side when no true crossover points appear and even then it may still underestimate the thickness if it has a time lower than the true crossover point.

When shots are close enough to the fault, that is when the fault is within the crossover distance of the shot such as nos 104 to 108, the first arrival consists of the direct wave followed by the head wave travelling along the half-space boundary on the right side of the fault, as shown by branches L1 to L3. The travel time curve for each individual shot does not show any anomalous features. However, the curves as a group are different from those for a continuous flat-layered structure. The intercept times do not remain constant, but increase systematically with distances away from the fault (from L1 to L3). This is as a result of the difference in the distance from the source to the fault. (Travel path for the pseudo–head-wave branches, such as L1, is shown in the bottom panel. It travels first from shot no. 104 to point U, then along the right interface and then back to

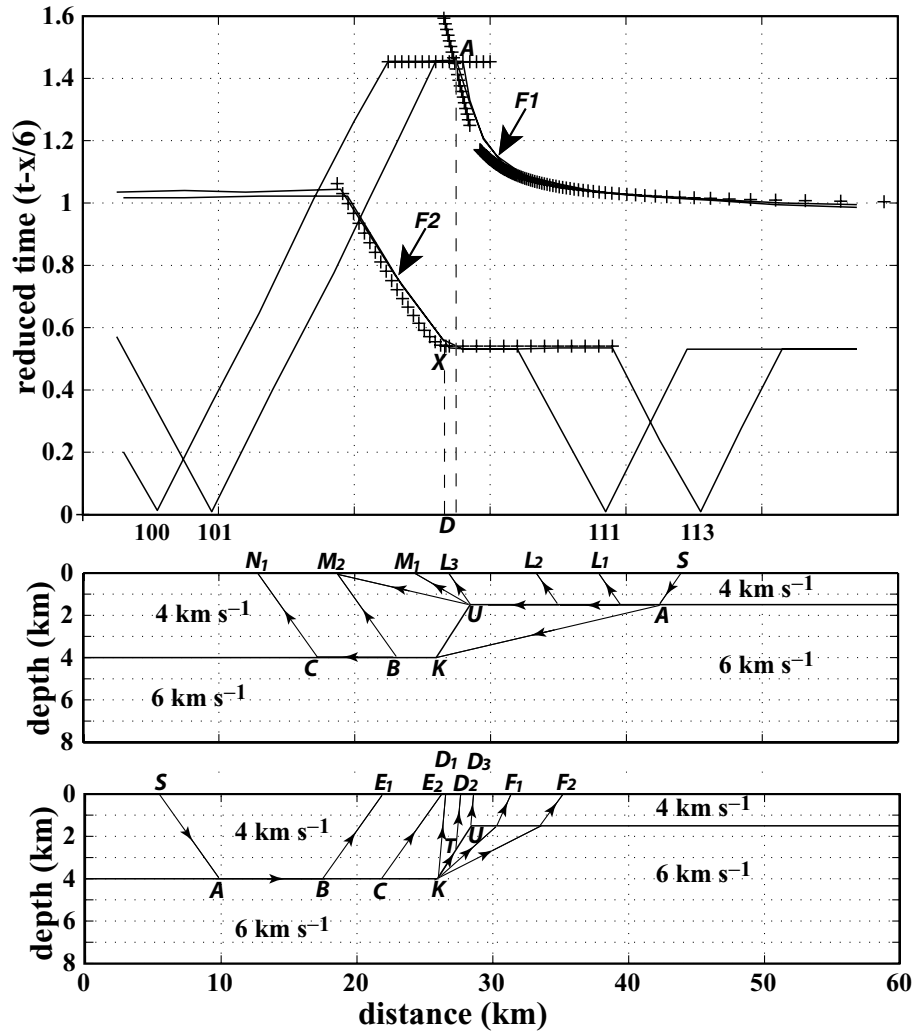

Figure A1. Velocity Models and synthetic first arrival picks for normal faulted and thrust faulted structures. In both plots, the solid line represents synthetic first arrivals from finite-difference modelling and the plus signs are the calculated travel times from ray theory. The ray paths for the calculation are shown in the lower two panels. F1 and F2 in the upper panel represent the two diagnostic features discussed in the Appendix. The middle panel shows the ray paths for different phases that appear as first arrivals for a shot on the hangingwall, while the bottom panel shows those for a shot on the footwall. The top layer thickness of the hangingwall is designated as h. Note that the location of F1 (point A) is normally controlled by point K in the model, while F2 (point X) is controlled by point U. On the left is for a normal fault with a dip angle of 45°. Note that the distance between points A and X is much smaller tha a vertical fault situation. Compare it with Fig. 5. Here, $D < h \tan \theta$. On the right is for a steep thrust faulted structure (dip angle is 45°); the distance between point A and X is $D > 2h \tan \theta$. Relative position of A and X does not vary much with the dip angle. For a normal fault situation, D varies with the dip angle: the smaller the dip angle, the smaller the distance. A and X might be aligned or in a reverse relative position for a shallow-dipping normal fault.

the surface.) This is another characteristic feature of faults (F3). We should note that we will significantly underestimate the thickness of the layer of the footwall if we use the intercept points of these branches to estimate the layer thickness beneath the shot. The intercept point of shot no. 108 should give a reasonable estimate of the layer thickness for the hangingwall side however.

For shots on the hangingwall side of the fault, such as nos 110 to 113, the first arrival branches exhibit a normal crossover point (E1–E3) but, at a point (X) just to the left of the fault, the travel time curves of all the shots converge to each other and adopt a low apparent velocity: a velocity that approaches asymptotically to the velocity of the layer on the left side. Eventually at about the crossover distance of the left side interface away from the shot, the head wave phase travelling along the left side half-space boundary appears as first arrival and the travel time curve adopts the half-space velocity. The relatively slow diffracted phase between the two fast phases is the third characteristic of faults (F2) and it is the result of the change of ray paths from head waves along the right interface to a diffracted phase from the point U in the model. We can use the true crossover points like E1 to E3 to get a correct estimate of the layer thickness of the hangingwall if they exist.

The ray paths that give rise to the above three features are shown as arrowed lines in the velocity model in Fig. 5. The middle panel shows the ray paths for the negative-slope segment ACM (F1). The bottom panel shows the reciprocal ray paths for shots from the footwall and the hangingwall. They give rise to the unusual low-velocity segment feature (F2) and the systematically increasing intercept time head wave branches (F3).

The important points in the model are the layer piercing points (U for the hangingwall side and K for the footwall side), which are closely related to the dip direction of the fault. The discontinuity of the interface in the velocity structure gives rise to the features in

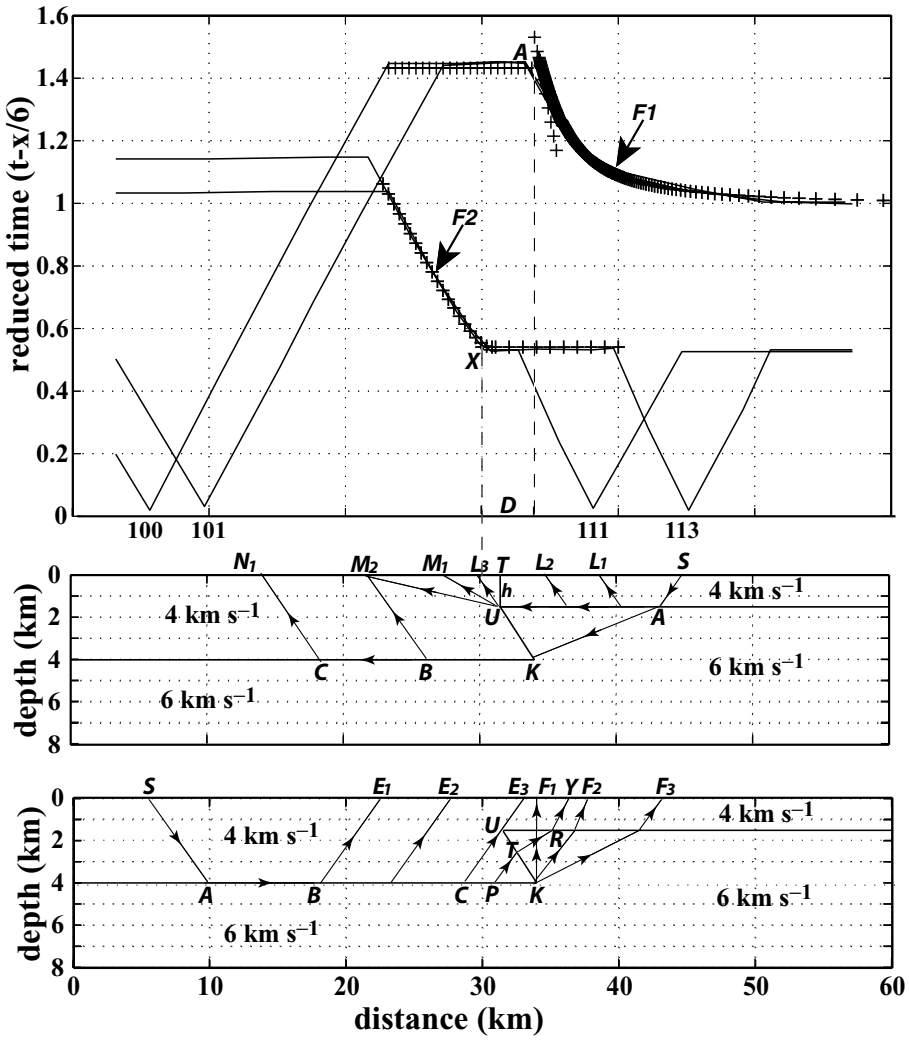

Figure A1. (*Continued*.)

the first arrival data described above and these break points control the location of the three features. Feature F1 depends on K, while features F2 and F3 depend on U. When the fault dips, these two points move laterally relative to one another, their corresponding features moving with them. For the vertical fault described above (Fig. 5), the kink point A of F1 is slightly to the hangingwall side of the fault and the kink point X of F2 is $h \tan \theta$ away from the fault, with a distance between them being in the range of $h \tan \theta < D < 2h \tan \theta$. Here h is the thickness for the hangingwall and θ is the critical angle.

For a steep normal faulted structure, the kink point A of F1 is on the footwall side, i.e. on the same side as U. This makes the distance between A and X much smaller than the vertical situation (compare Figs 5 and A1a). The two points might be aligned to the same ground point as is the case for the Pelona fault or even reverse relative position when the dip angle of the fault gets shallower.

If the fault is a thrust fault (Fig. A1b), the kink point A of F1 is located considerably (at least $h \tan \theta$) to the hangingwall side of the fault. The position of point A in the arrival data is also controlled by point U in the model and the distance between the two kink points (X and A) is almost independent of the dip angle of the fault, with a value bigger than $2h \tan \theta$. As the dip angle gets smaller, the amplitude of the pulses consists of feature F2 in the waveform data gets smaller and almost invisible for a 30°-dipping fault. From our finite difference modelling, amplitudes of the segment F2 are generally much smaller for a thrust faulted structure than that of a vertical or normal fault situation. Two synthetic seismograms for a thrust fault and normal fault are shown in Fig. A2.

In Fig. A1, the plus signs (+) denote travel time computed using the rays in the lower panels of the figures. They compare well to the travel times denoted by the solid lines, which are determined by finite-difference modelling.

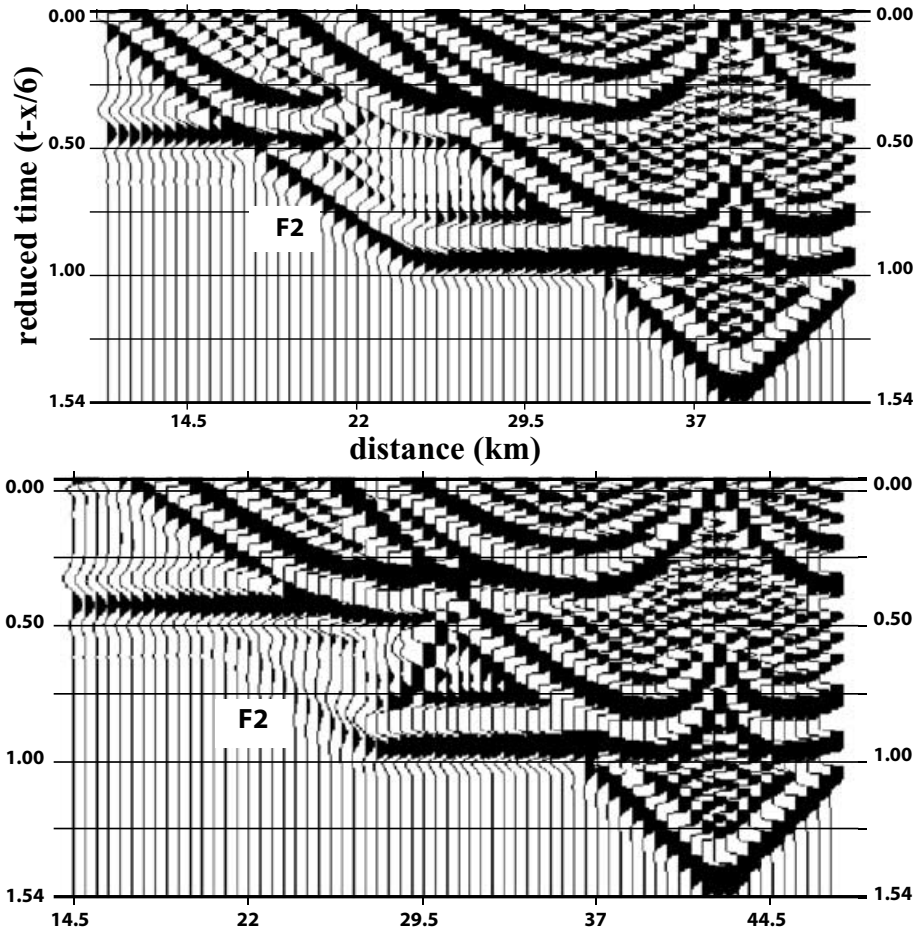

Figure A2. Amplitude comparison of the segment F2 for the two faulted structure above. Synthetic seismogram for the normal fault is shown on the top, while one synthetic shot gather from the thrust faulted structure is shown on the bottom. Note the amplitude difference for the segment F2. The amplitude for the normal case is much higher than that for the thrust fault. This amplitude difference is helpful in estimating the dip directions of faults for seismic surveys.